IOPscience iopscience.iop.org

Home Search Collections Journals About Contact us My IOPscience

Differential kinetic dynamics and heating of ions in the turbulent solar wind

This content has been downloaded from IOPscience. Please scroll down to see the full text.

2016 New J. Phys. 18 125001

(http://iopscience.iop.org/1367-2630/18/12/125001)

View the table of contents for this issue, or go to the journal homepage for more

Download details:

IP Address: 160.97.1.247
This content was downloaded on 02/12/2016 at 13:50

Please note that terms and conditions apply.

New Journal of Physics
The open access journal at the forefront of physics

Deutsche Physikalische Gesellschaft DPG
IOP Institute of Physics

Published in partnership with: Deutsche Physikalische Gesellschaft and the Institute of Physics

OPEN ACCESS

RECEIVED
21 September 2016

REVISED
14 November 2016

ACCEPTED FOR PUBLICATION
15 November 2016

PUBLISHED
2 December 2016

Original content from this work may be used under the terms of the Creative Commons Attribution 3.0 licence.

Any further distribution of this work must maintain attribution to the author(s) and the title of the work, journal citation and DOI.

PAPER

Differential kinetic dynamics and heating of ions in the turbulent solar wind

F Valentini[1], D Perrone[2], S Stabile[1], O Pezzi[1], S Servidio[1], R De Marco[3], F Marcucci[3], R Bruno[3], B Lavraud[4,5], J De Keyser[6], G Consolini[3], D Brienza[3], L Sorriso-Valvo[7], A Retinò[8], A Vaivads[9], M Salatti[10] and P Veltri[1]

[1] Dipartimento di Fisica, Università della Calabria, Rende (CS), I-87036, Italy
[2] European Space Agency, Science and Robotic Exploration Directorate, ESAC, Madrid, Spain
[3] INAF-IAPS Istituto di Astrofisica e Planetologia Spaziali, I-00133 Roma, Italy
[4] Institut de Recherche en Astrophysique et Planétologie, Universit de Toulouse, France
[5] Centre National de la Rescherche Scientifique, UMR F-5277, Toulouse, France
[6] Royal Belgian Institute for Space Aeronomy, B-1180, Brussels, Belgium
[7] CNR-Nanotec, Rende (CS), I-87036, Italy
[8] Laboratoire de Physique des Plasmas, Ecole Polytechnique, Palaiseau, F-91128, France
[9] Swedish Institute of Space Physics, Uppsala, SE-75121, Sweden
[10] Agenzia Spaziale Italiana, I-00133 Roma, Italy

E-mail: francesco.valentini@fis.unical.it

Keywords: solar wind, turbulence, plasma heating, space missions

Abstract

The solar wind plasma is a fully ionized and turbulent gas ejected by the outer layers of the solar corona at very high speed, mainly composed by protons and electrons, with a small percentage of helium nuclei and a significantly lower abundance of heavier ions. Since particle collisions are practically negligible, the solar wind is typically not in a state of thermodynamic equilibrium. Such a complex system must be described through self-consistent and fully nonlinear models, taking into account its multi-species composition and turbulence. We use a kinetic hybrid Vlasov–Maxwell numerical code to reproduce the turbulent energy cascade down to ion kinetic scales, in typical conditions of the uncontaminated solar wind plasma, with the aim of exploring the differential kinetic dynamics of the dominant ion species, namely protons and alpha particles. We show that the response of different species to the fluctuating electromagnetic fields is different. In particular, a significant differential heating of alphas with respect to protons is observed. Interestingly, the preferential heating process occurs in spatial regions nearby the peaks of ion vorticity and where strong deviations from thermodynamic equilibrium are recovered. Moreover, by feeding a simulator of a top-hat ion spectrometer with the output of the kinetic simulations, we show that measurements by such spectrometer planned on board the Turbulence Heating ObserveR (THOR mission), a candidate for the next M4 space mission of the European Space Agency, can provide detailed three-dimensional ion velocity distributions, highlighting important non-Maxwellian features. These results support the idea that future space missions will allow a deeper understanding of the physics of the interplanetary medium.

1. Introduction

The solar wind is a rarefied, highly variable flow of charged particles originating from the Sun. This medium is composed mainly by electrons and protons, with a small fraction of alpha particles (helium nuclei) and a lower percentage of heavier ions. Due to its low particle density, collisions are essentially negligible, and the solar wind plasma is in a state of non-thermodynamic equilibrium [1]. One of the most puzzling aspects of the solar wind dynamics consists in the empirical evidence [2] that it is hotter than expected from adiabatic expansion [2–4]. Understanding the mechanisms of energy dissipation and particle heating in such a collisionless system represents a real challenge for space plasma physics.

© 2016 IOP Publishing Ltd and Deutsche Physikalische Gesellschaft

'*In situ*' spacecraft measurements reveal that the solar wind is in a state of fully-developed turbulence [5, 6]. The energy injected by large scale solar dynamical features into the Heliosphere, in the form of long-wavelength fluctuations, cascades towards small scales via nonlinear interactions until it can be transferred to the plasma as heat. In the inertial range, the power spectrum of the solar wind fluctuations manifests a behavior reminiscent of the Kolmogorov phenomenology for fluid turbulence [7–11]. The turbulent cascade extends to smaller spatial scales, down to a range of wavelengths where kinetic effects start playing a non-negligible role. At the typical ion characteristic scales (Larmor radius and/or inertial length), different physical processes come into play, leading to changes in the spectral shape [12–19]. Here, the dynamics of the solar wind ions gets extremely complicated, being dominated by complex kinetic processes such as resonant wave-particle interactions, particle heating, generation of temperature anisotropy, production of beams of accelerated particles, etc. In this range of scales the particle velocity distribution is generally observed to deviate from the typical Maxwellian shape of thermodynamic equilibrium.

Several models have been developed to understand the kinetic scale phenomenology, focusing specifically on heating and acceleration processes. To explain the above phenomena, several physical mechanisms have been proposed. Among them, the ion-cyclotron resonance can produce heating [20–27], where ions interact resonantly with ion-cyclotron waves generated along the cascade. An alternative model is the non-resonant stochastic heating [28, 29], where the fluctuations at scales comparable with the ion gyro-scales produce significant distortions of the ion orbits that become stochastic in the plane perpendicular to the magnetic field, violating the magnetic moment conservation. Finally, it has been clearly observed that the interaction of particles with coherent structures can locally produce heating and non-Maxwellian features [30–36].

One of the most relevant aspects of the ion heating process in the solar wind is that the heavy ions are preferentially heated and accelerated with respect to protons. Measurements of solar wind hydrogen and helium temperatures [37] show compelling evidence of Alfvén-cyclotron dissipation mechanisms. A more recent observational study [38] shows that for the heavy ion component ($A > 4$ amu) the temperature displays a clear dependence on mass, probably reflecting the physical conditions in the solar corona. Again, the interpretation of these observations is mostly based on the physical processes of wave-particle interactions [39–48], stochastic ion heating [49], and interaction between particles and coherent structures [50–52]. Despite a significant theoretical effort, there is still no definitive solution to the problem of heavy ions differential heating. It is important to note that the physical processes of the differential heating of heavy ions are also important for laboratory plasmas research, aiming at heating a confined plasma to initiate fusion reactions.

In this paper, we study the kinetic dynamics of protons and alpha particles in typical conditions of the interplanetary medium, by employing multi-component Eulerian hybrid Vlasov–Maxwell (HVM) simulations [40, 53]. The multicomponent version of the HVM code integrates the Vlasov equation numerically for the distribution function of both protons and alpha particles, while treating electrons as a massless, isothermal fluid. We present the numerical results of HVM simulations of decaying turbulence with guide field, in a 2D-3V phase space domain (two-dimensions in physical space and three-dimensions in velocity space). During the turbulent cascade, the ion species depart locally from the condition of thermodynamic equilibrium [33, 50, 54–56], exhibiting temperature anisotropy, differential kinetic behavior as well as preferential heavy ion heating. Interestingly, the preferential heating process occurs in thin filaments of the typical size of few inertial lengths, preferentially located in the proximity of vorticity structures. In the same regions, significant deviations from Maxwellian distributions are observed for ion species. Moreover, as we will discuss in detail below, we have analyzed the distribution of the numerical data in the fire-hose and mirror stability plane, as dependent on the multi-ion composition of the interplanetary medium, showing a good agreement between the numerical results and the observational evidences discussed in a recent paper by Chen *et al* [57].

Finally, through a top-hat simulator [58] using the output of the HVM simulations, we show that the cold solar wind (CSW) instrument [59] on board the Turbulence Heating ObserveR—THOR spacecraft [60], a candidate for the next M4 space mission of the European Space Agency, is able to provide adequate high resolution measurements of the ion velocity distributions for the study of turbulent ion heating. In this regard, the THOR mission will allow to measure the velocity distributions of the solar wind protons and alpha particles, with unprecedented phase space resolution.

2. Setup of multi-ion HVM simulations

To perform a numerical study of the microphysics of a multi-ion turbulent plasma, we employ an Eulerian HVM numerical code [50, 53] which solves the Vlasov equations for the distribution functions of protons and alpha particles. In this model electrons are treated as an isothermal massless fluid. Vlasov equations for ions are coupled to a generalized Ohm's law, in which both the Hall term and the electron pressure contribution are retained, and to the Ampére and Faraday equations. The displacement current is neglected and quasi-neutrality

Table 1. Simulation parameters.

RUN	$\beta_p = 2v_{\mathrm{th},p}^2/V_\mathrm{A}^2$	$\delta B/B_0$	$t^*\Omega_\mathrm{cp}$
1	0.5	1/3	49
2	2.0	1/3	51
3	1.0	2/3	25

is assumed. The dimensionless HVM equations can be written as:

$$\frac{\partial f_s}{\partial t} + \mathbf{v}\cdot\frac{\partial f_s}{\partial \mathbf{r}} + \xi_s(\mathbf{E}+\mathbf{v}\times\mathbf{B})\cdot\frac{\partial f_s}{\partial \mathbf{v}} = 0, \tag{1}$$

$$\mathbf{E} = -(\mathbf{u}_e\times\mathbf{B}) - \frac{1}{n_e}\nabla P_e + \eta\mathbf{j}, \tag{2}$$

$$\frac{\partial \mathbf{B}}{\partial t} = -\nabla\times\mathbf{E}. \tag{3}$$

In the above equations, masses and charges have been scaled by the proton mass m_p and charge e respectively, time by the inverse proton-cyclotron frequency ($\Omega_\mathrm{cp}^{-1} = m_p c/eB_0$, B_0 being the ambient magnetic field and c the speed of light), velocity by the Alfvén speed ($V_\mathrm{A} = B_0/\sqrt{4\pi n_{0,p} m_p}$, $n_{0,p}$ being the equilibrium proton density), in which we only considered the contribution of the dominant proton species, and length by the proton skin depth ($d_p = V_\mathrm{A}/\Omega_\mathrm{cp}$). In equation (1), $f_s(\mathbf{r},\ \mathbf{v},\ t)$ is the ion distribution function (the subscript $s = p,\ \alpha$ refers to protons and alpha particles, respectively), $\mathbf{E}(\mathbf{r},\ t)$ and $\mathbf{B}(\mathbf{r},\ t)$ are the electric and magnetic fields, and ξ_s is a constant that depends on the charge to mass ratio of each ion species ($\xi_p = 1$ and $\xi_\alpha = 1/2$). In equation (2), the electron bulk velocity $\mathbf{u}_e$ is defined as $(\Sigma_s Z_s n_s \mathbf{u}_s - \mathbf{j})/n_e$, where Z_s is the ion charge number ($Z_p = 1$ and $Z_\alpha = 2$), the density n_s and the ion bulk velocity $\mathbf{u}_s$ are 0th and first order velocity moment of the ion distribution function, respectively. The electron density is derived from the quasi-neutrality equation $n_e = \Sigma_s Z_s n_s$. Furthermore, $\mathbf{j} = \nabla\times\mathbf{B}$ is the total current density and $P_e = n_e T_e$ is the electron pressure (T_e is assumed to be constant in time and space). A small resistive term has been added as a standard numerical Laplacian dissipation ($\eta = 2\times10^{-2}$), in order to remove any spurious numerical effects due to the generation of strong magnetic field gradients during the development of turbulence.

We solve the multi-ion HVM equations in a 2D-3V phase space domain. The system size in the spatial domain is $L = 2\pi\times 20 d_p$ in both x and y directions, where periodic boundary conditions have been implemented, while the limits of the velocity domain are fixed at $v_{\mathrm{max},s} = \pm 5 v_{\mathrm{th},s}$ in each velocity direction, $v_{\mathrm{th},s} = (k_B T_{0,s}/m_s)^{1/2}$ being the ion thermal speed at equilibrium and $T_{0,s}$ the equilibrium temperature. In each direction in the velocity domain we set $f_s(|v| > v_{\mathrm{max},s}) = 0$. The 5D numerical box has been discretized by 512^2 grid-points in the 2D spatial domain and 71^3 grid-points in both proton and alpha-particle 3D velocity domains. A higher velocity resolution has been adopted here with respect to previous works [50, 51], in order to ensure a significantly improved conservation of the Vlasov invariants and to provide a better description of the details of the ion distribution function in velocity space. The time step, Δt, has been chosen in such a way that the Courant–Friedrichs–Lewy condition for the numerical stability of the Vlasov algorithm is satisfied [61]. In order to control numerical accuracy, a set of conservation laws is monitored during the simulations: typical relative variations of the total energy is $\simeq$0.6%, of the entropy is $\simeq$0.4% and of the mass is $\simeq 2.5\times10^{-3}$% for protons and $\simeq$0.35% for alpha particles.

At $t = 0$, both ion species have Maxwellian velocity distributions and homogeneous constant densities. To simulate physical conditions close to those of the pristine solar wind, at equilibrium we set the alpha particle to proton density ratio $n_{0,\alpha}/n_{0,p} = 5\%$ and temperature of each species such that $T_{0,\alpha} = T_{0,p} = T_e$. The plasma is embedded in a uniform background out of plane magnetic field, $\mathbf{B}_0$ ($\mathbf{B}_0 = B_0\hat{\mathbf{e}}_z$). We perturb the initial equilibrium with a 2D spectrum of Fourier modes, for both proton bulk velocity and magnetic field. The energy is injected with random phases and wave numbers in the range $0.1 < k < 0.3$, where $k = 2\pi m/L$, with $2 \leqslant m \leqslant 6$. Neither density disturbances nor parallel variances are imposed on the initial equilibrium, namely $\delta n = \delta u_z = \delta B_z = 0$. We performed three different simulations whose relevant parameters are summarized in table 1. Below, we will discuss the results of RUN 1. RUN 2 and RUN 3 are qualitatively similar to RUN 1 and have been considered to have significant statistics to perform a direct comparison with solar wind data.

3. Turbulence cascade and generation of temperature anisotropy

We numerically investigate the kinetic evolution of protons and alpha particles in a situation of decaying turbulence. The large scale fluctuations imposed on the initial equilibrium produce a turbulent cascade down to

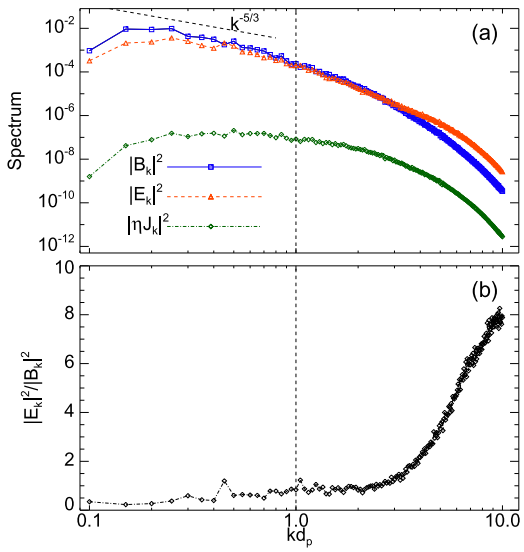

Figure 1. Panel (a): omni-directional spectra of magnetic (blue solid-square line) and electric (red dashed-triangle line) energy at the maximum of the turbulent activity. Panel (b): semi-logarithmic plot of the ratio between electric and magnetic energy. The vertical black dashed lines indicate the proton skin depth characteristic wavenumber. The Kolmogorov expectation, $k^{-5/3}$, is reported as a black dashed line, while the green diamond curve represents the contribution $|\eta J_k|^2$ to the electric energy, due to the resistive term in the Ohm's law in equation (2).

kinetic scales. In analogy with fluid models, by looking at the time evolution of the spatially averaged mean squared out of plane current density $\langle j_z^2 \rangle$, it is possible to identify an instant of time t^* at which the turbulent activity reaches its maximum level [62]. The value of t^* in units of Ω_{cp}^{-1} is reported in the right column of table 1, for each simulation. At this time t^* we perform our analysis [33, 50, 54, 56].

In panel (a) of figure 1, we show the omni-directional magnetic $|B_k|^2$ (blue solid-square line) and electric $|E_k|^2$ (red dashed-triangle line) spectra at $t = t^*$ for RUN 1. The Kolmogorov expectation, $k^{-5/3}$ (black dashed line), is reported as a reference, while the vertical black dashed line indicates the proton skin depth characteristic wavenumber. In the range of small wavenumbers the magnetic activity is dominant, while the situation clearly changes for $kd_p > 2$, where the electric energy becomes larger than the magnetic one. To highlight this point, in panel (b) of figure 1 we report the electric to magnetic energy ratio as a function of the wavenumber. The break point between the two regimes is located around the proton skin depth, where dispersive Hall effects come into play [54]. These results present several similarities to spacecraft measurements in the solar wind [15, 63, 64].

As already noticed in previous works [33, 50, 51, 54, 56], ion temperature anisotropy is generated along the development of the turbulent cascade. We focus, at first, on the temperature anisotropy with respect to the direction of the local magnetic field $T_\perp/T_\parallel$ for each ion species. The temperature of each ion species has been computed as the second-order velocity moment of the ion distribution function:

$$T_s = \frac{m_s}{3n_s} \int (\mathbf{v} - \mathbf{u}_s)^2 f_s \mathrm{d}^3 v \quad s = p, \alpha. \tag{4}$$

In figure 2, we show the 2D contours of the temperature anisotropy of protons (left) and alpha particles (right) at $t = t^*$, for RUN 1 (the same behavior is observed for RUN 2 and RUN 3); as can be noticed from the comparison of both panels of this figure, the global bi-dimensional patterns of the temperature anisotropy display similar features, with larger values of anisotropy being concentrated in thin filaments (of the typical size of few ion skin depths) for both species. However, a significant differential behavior is observed, as the alpha particles appear consistently more anisotropic than the protons.

With the aim of showing that the numerical results of the ensemble of simulations in table 1 reproduce closely the typical behavior observed in the solar wind multi-ion plasma, we consider here a recent paper by Chen *et al* [57], in which solar wind ion temperature anisotropy from the *Wind* spacecraft at 1AU has been analyzed. The authors proposed a detailed study of the plasma stability, as dependent on the simultaneous presence of protons, electrons and alpha particles, as main constituents of the solar wind plasma. Specifically, they made a comprehensive analysis based on three years of data and gave clear evidence that the fire-hose and mirror instability thresholds, calculated in [65, 66] for a multi-species plasma system, well constrain the whole data distribution to the stable side and that the contours of the distribution follow the shape of the thresholds.

In order to compare with these observations, we have considered the conditions for the long-wavelength fire-hose and mirror instabilities in a multi-species plasma [65, 66]:

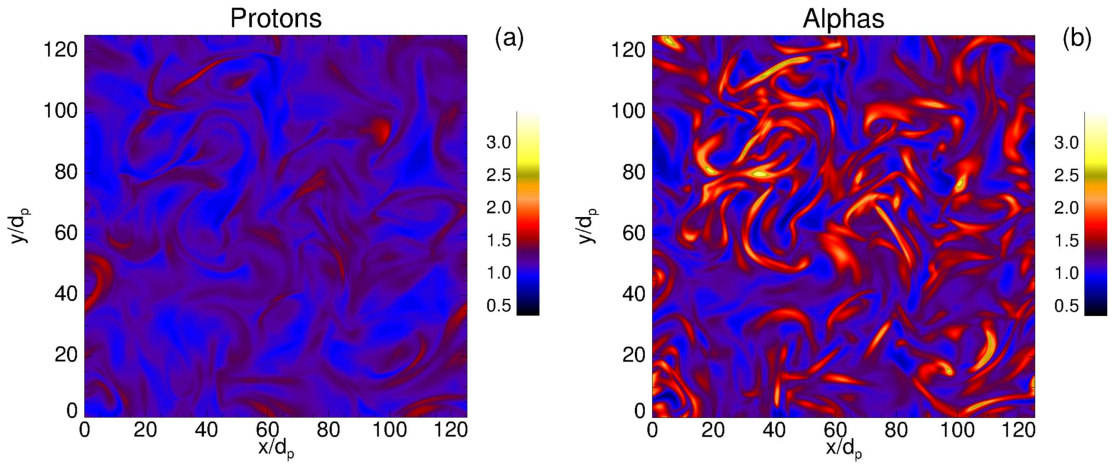

Figure 2. 2D contour plot of the temperature anisotropy $T_\perp/T_\parallel$ with respect to the direction of the local magnetic field for protons (a) and alpha particles (b).

$$\Lambda_f = \frac{\beta_\parallel - \beta_\perp}{2} + \frac{\sum_s \rho_s |\Delta \mathbf{v}_s|^2}{\rho v_A^2} > 1, \tag{5}$$

$$\Lambda_m = \sum_s \beta_{\perp s}\left(\frac{\beta_{\perp s}}{\beta_{\parallel s}} - 1\right) - \frac{\left(\sum_s q_s n_s \beta_{\perp s}/\beta_{\parallel s}\right)^2}{2\sum_s (q_s n_s)^2/\beta_{\parallel s}} > 1, \tag{6}$$

where s stands for protons, alphas and electrons respectively ($s = p,\ \alpha,\ e$), $\beta_{\perp,\parallel} = \sum_s \beta_{\perp,\parallel s}$ is the plasma beta in the direction perpendicular and parallel to the local magnetic field, ρ_s is the mass density of the species s, ρ is the total mass density, v_A is the local Alfvén speed, $\Delta \mathbf{v}_s$ is the difference between the bulk velocity of the species s and the center of mass velocity. In figure 3 (panel (a)) we report a scatter plot of the first and second term of Λ_f (logarithmic axes), for all the cases in table 1. Data are clearly constrained in the stable region (delimited by the solid line). These numerical results are in agreement with the solar wind analysis, as can be seen comparing our study with figure 2 of [57]. This further confirms that the HVM model can describe the basic dynamics of the solar wind ion species. However, in this direct comparison one has to take into account the limitations of the approximation of isothermal (massless fluid) electrons, and limitations in the statistical convergence (data produced by three numerical runs cannot fully recover the statistics of three years of spacecraft measurements). In panels (b) and (c) of figure 3, we show $\log_{10}\Lambda_f$ and $\log_{10}\Lambda_m$ respectively, as a function of $\log_{10}\beta$, β being the total plasma beta. Here, one can easily see that the instability thresholds (black-dashed lines) are reached for $\beta \geqslant 1$, again in good agreement with figure 5 of [57].

4. Coherent structures, kinetic effects and differential heating

During the development of the turbulence cascade, temperature increase is observed for both ion species, alpha particles being preferentially heated with respect to protons. Moreover, the generation of ion temperature anisotropy discussed in the previous section is associated to the appearance of coherent structures, such as current sheets, filaments, strongly sheared flows, etc, observed in the 2D patterns in physical space. In particular, panel (a) of figure 4 displays the shaded contours of the out of plane current density j_z at $t = t^*$ for RUN 1, together with the contour lines of the magnetic potential A_z of the in-plane magnetic field ($\mathbf{B}_\perp = \nabla A_z \times \mathbf{e}_z$). Magnetic flux tubes with different polarizations (or magnetic islands in 2D) are identified by closed contours of A_z, as it can be seen from panel (a) of this figure. As it is clear from this contour plot, current density becomes very intense in between adjacent magnetic islands. We point out that the mirror and fire hose unstable points in figures 3(b)–(c) (obtained in RUN 3, with increased initial magnetic perturbations) are located in spatial positions very close to strong current sheets. In panel (b) of figure 4 we show the contour map of the proton to alpha particle temperature ratio. Even though at $t = 0$ ions have been initialized with equal temperature ($T_{0,p} = T_{0,\alpha}$), during the evolution of turbulence, the alpha particles are heated preferentially with respect to protons. Moreover, the 2D map shows that the differential heating is not uniform, but is strongly inhomogeneous, displaying a pattern similar to the 2D map of j_z and being significantly influenced by the topology of the magnetic field [33, 35, 51, 54, 56]. Moreover, the physical mechanism responsible for the ion heating process is evidently more efficient for the alpha particles than for the protons.

As the HVM code allows for a clean and almost noise-free description of the ion distribution function in phase space, we can analyze the kinetic dynamics of the ion species associated to the development of the

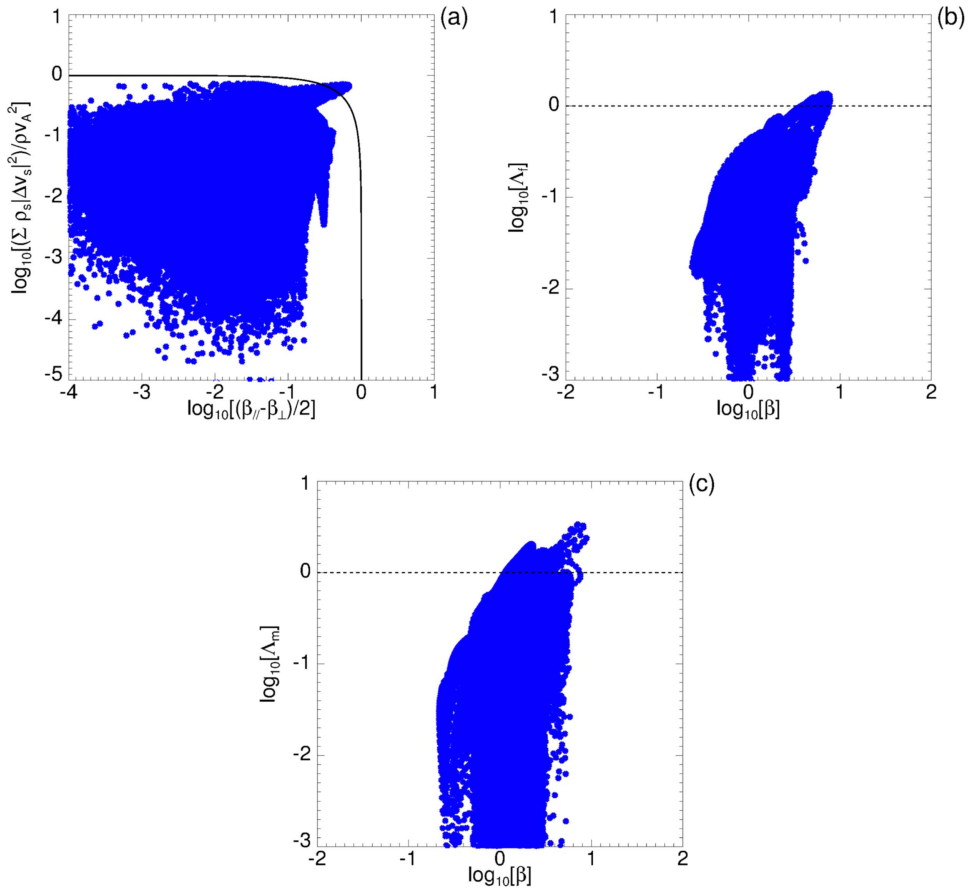

Figure 3. (a) Scatter plot of the two terms of Λ_f for the ensemble of simulations in table 1. Solid (black) line represents the instability threshold. Panels (b) and (c): $\log_{10}\Lambda_f$ and $\log_{10}\Lambda_m$, respectively, as a function of $\log_{10}\beta$.

turbulent cascade and to the differential ion heating. Several '*in situ*' observations (see, for instance, [1, 67]) and previous numerical simulations [33, 43, 50, 51, 54–56, 68, 69] have shown that the ion distribution functions in the turbulent solar wind (especially in the less collisional fast wind) are typically far from thermodynamical equilibrium and that kinetic effects manifest through the appearance of field-aligned beams of accelerated particles, generation of ring-like modulations in the particle velocity distributions and, in general, through complicated non-Maxwellian deformations. In order to quantify the deviation of the ion velocity distributions from the Maxwellian shape in our simulations, we introduce the following non-Maxwellian measure [34], for each ion species:

$$\epsilon_s = \frac{1}{n_s}\sqrt{\int (f_s - g_s)^2 \mathrm{d}^3 v}\,, \tag{7}$$

where g_s is the associated equivalent Maxwellian distribution computed from the parameters of f_s [34]. We point out that at $t = 0$, ϵ_s is null, since both ion species have been initialized with a Maxwellian velocity distribution. We observe that, simultaneously with the evolution of turbulence, the ion distributions dramatically deviate from the Maxwellian shape. Panels (c) and (d) of figure 4 display the contour maps of ϵ_s for protons and alpha particles, respectively, at $t = t^*$ for RUN1. As it is clear from this figure, both ion species significantly deviate from thermodynamic equilibrium and the spatial distribution of ϵ_s is not uniform, displaying features quite similar to the 2D contours of the out of plane current density (panel (a)) and of the ion temperature ratio (panel (b)). In particular, kinetic effects seem to be localized near the peaks of the current density in the shape of thin filaments. It is worth noting that deviations from Maxwellian are significantly stronger for the alpha particles than for the protons; that is, larger values of ϵ_α are recovered with respect to ϵ_p and are achieved in spatial positions close to peaks of the current density, where differential heating is also observed.

Ion differential heating usually occurs close to thin current sheets. Panels (a) and (b) of figure 5 report the y profile of j_z^2 (red-dashed curves), in two different ranges $y \in [3,\ 7]d_p$ and $y \in [116,\ 122]d_p$, computed at $x \sim 50d_p$ and $x \sim 110d_p$, respectively. Two current sheets of typical width of a few proton skin depths are visible here. The black-solid curves in the same panels represent the corresponding y profile of T_α/T_p. As can be seen in the two panels, differential heating is observed close to each strong current sheet. However, the behavior

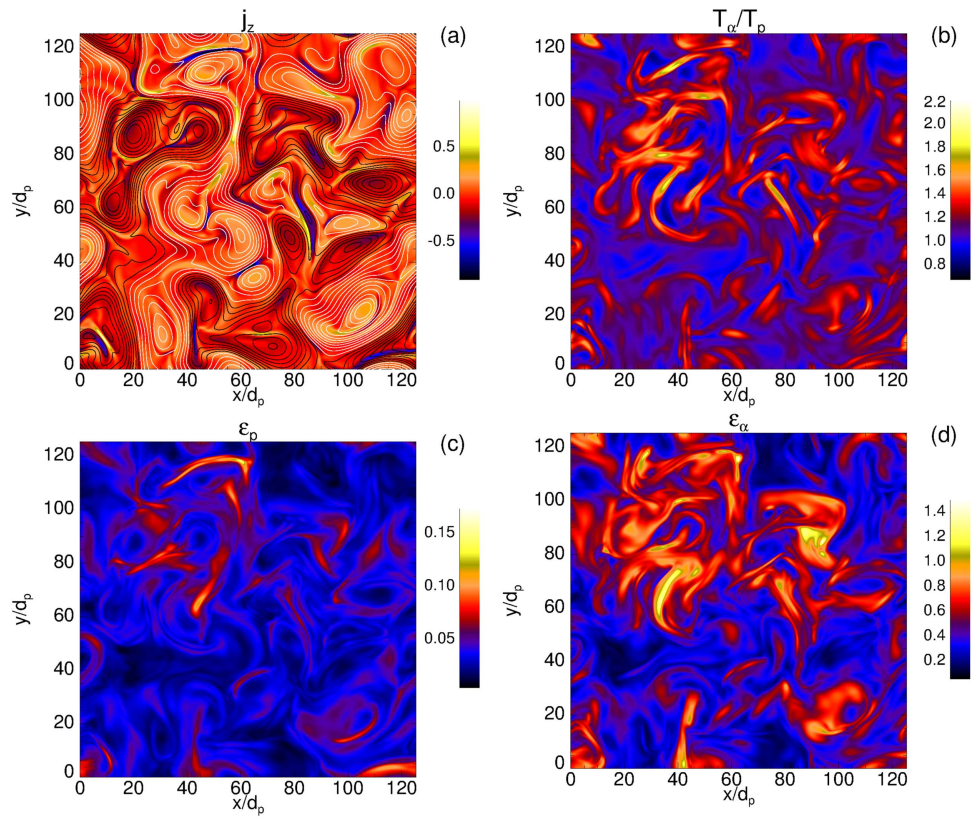

Figure 4. (a) Out of plane current density j_z. The isolines of the magnetic potential A_z are indicated by (black/white) lines. (b) Ratio between alpha particle and proton temperatures. Panels (c) and (d): ϵ for both protons and alpha particles, respectively. Each contour map is at the maximum of the turbulent activity.

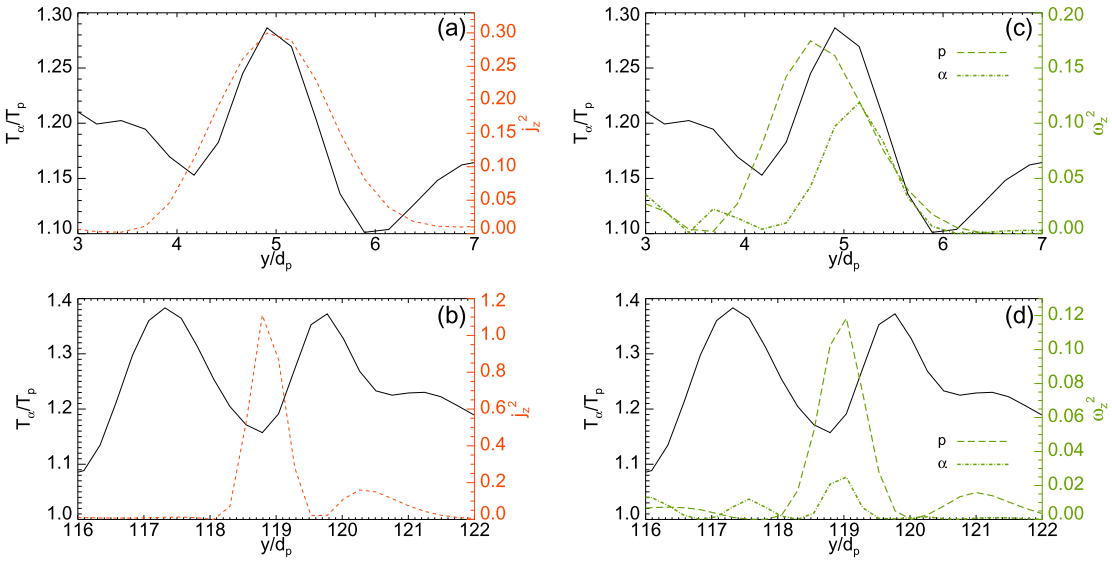

Figure 5. Spatial profiles of the squared current density j_z^2 (red dashed line, panels (a) and (b)) and of the squared vorticity ω_z^2 for protons (green dashed line, panels (c) and (d)) and for alpha particles (green dot-dashed line, panels (c) and (d)). In all panels, the alpha particle to proton temperature ratio is also shown (black solid line). All profiles are evaluated along the y direction at two different fixed spatial points: $x \sim 110 d_p$ (panels (a) and (c)) and $x \sim 50 d_p$ (panels (b) and (d)).

of the alpha to proton temperature ratio looks different in the two cases: in panel (a), alpha particles are preferentially heated in the center of the current sheet, while in panel (b) the differential heating occurs on both edges of the current sheet. This is a quite general behavior, in the sense that, close to each coherent current structure identified in the spatial domain, the alpha to proton temperature ratio displays a peak in the middle of

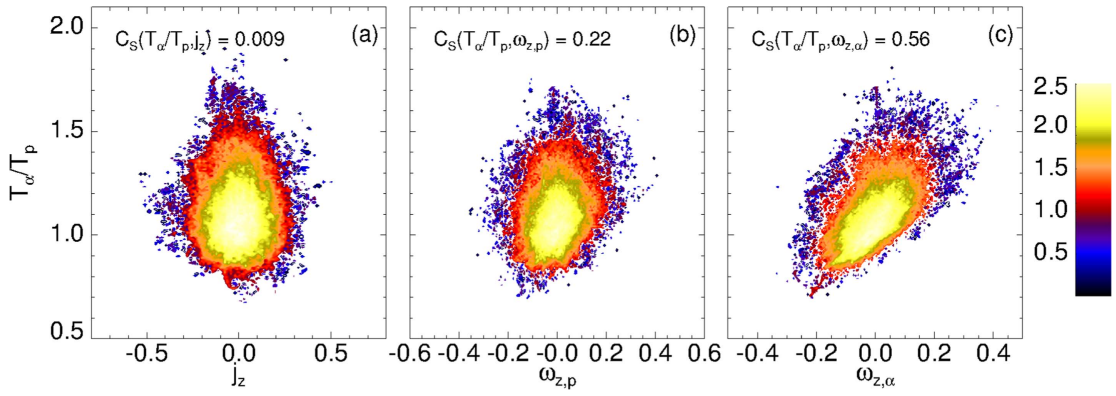

Figure 6. From left to right: the joint probability distributions $P(T_\alpha/T_p,\ j_z)$, $P(T_\alpha/T_p,\ w_{z,p})$, and $P(T_\alpha/T_p,\ \omega_{z,\alpha})$, in $\log_{10}$ scale. The corresponding Spearman correlation coefficients are indicated in each plot.

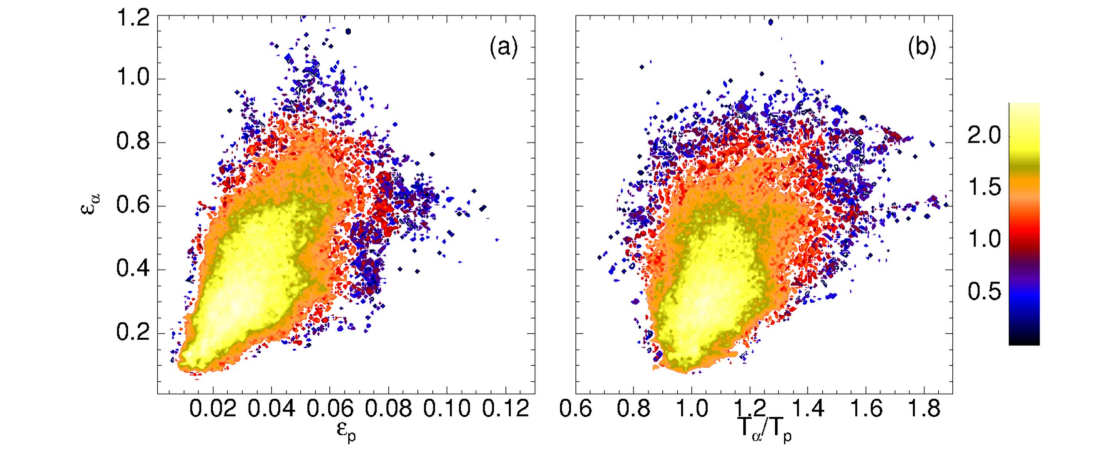

Figure 7. Joint probability distributions of ϵ_α and ϵ_p (a) and of ϵ_α and T_α/T_p (b), in $\log_{10}$ scale, for RUN 1 at $t = t^*$.

the current sheet (as in panel (a)) or two peaks at its boundaries (as in panel (b)). Panels (c) and (d) of the same figure show similar plots for the squared vorticity component z associated to the proton velocity, $\omega^2_{z,p}$, and to the alpha particle velocity, $\omega^2_{z,\alpha}$ where $\boldsymbol{\omega} = \nabla \times \mathbf{v}$, at the same two positions as for the current j_z^2. The correlation observed for the vertical current is also clearly present for the vorticity.

The robustness of the correlation observed between the quantities shown in figure 5 can be visualized by means of the joint probability distributions $P(T_\alpha/T_p,\ j_z)$ and similarly for the vorticity $P(T_\alpha/T_p,\ \omega_z)$, as shown in figure 6. In the left panel, it is evident that there is actually no statistical correlation between the current and the differential heating, because of the spatial shift discussed above. On the contrary, an higher correlation is visible between the proton vorticity and the differential heating (central panel of figure 6). Even a stronger correlation is observed with the alpha-particle vorticity (right panel). A more quantitative assessment can be obtained by estimating the Spearman correlation coefficients between the alpha-proton temperature ratio and the current, $C_S(T_\alpha/T_p,\ j_z)$, and similarly for the two vorticity fields, as reported in each panel of figure 6. This observation suggests that the vortical motion of the alpha particles may play a significant role in, or may be significantly affected by, the differential heating process [70]. This correlation can be understood also in terms of magnetic reconnection. Topologically, magnetic reconnection might form quadrupolar vortical structures located near the current peak, as clearly shown in [71]. In these regions, both magnetic and velocity shears can trigger non-Maxwellian and thermal processes. A deeper analysis of the relationship of current and vortex structures with collisionless plasma heating can be found in [72].

At this point, it is important to better quantify the connection between the differential particle heating and the level of kinetic activity. In figure 7 we show the joint distributions of ϵ_α and ϵ_p (left panel) and of ϵ_α and T_α/T_p (right panel) for RUN 1 at $t = t^*$. Both panels show that (i) alpha and proton velocity distributions tend to deviate from Maxwellian at similar spatial locations, and (ii) such a deviation is correlated with the differential heating. In figure 8, the joint distribution of ϵ_p and ϵ_α has been conditioned to specific ranges of values of the

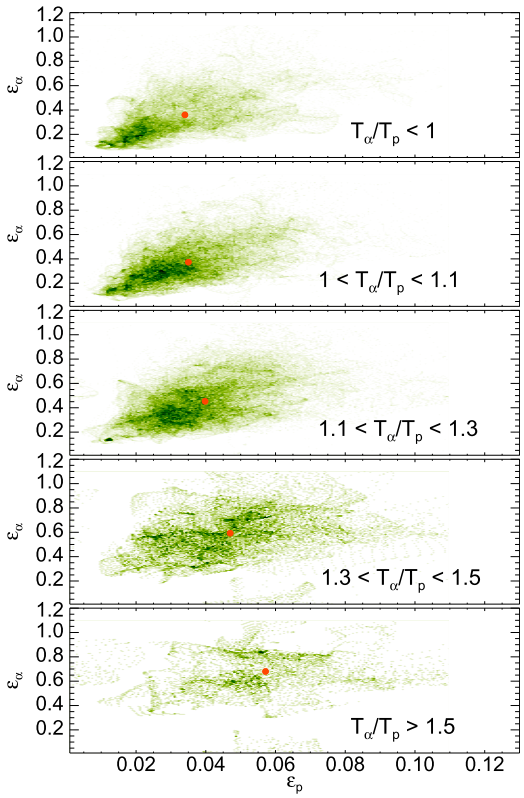

Figure 8. Conditioned joint distributions $P(\epsilon_\alpha, \epsilon_p|T_\alpha/T_p)$, for five bins of the conditioning variable T_α/T_p (increasing values from top to bottom); the location of the average value of T_α/T_p is indicated by a red dot in each panel. Each distribution is normalized to its peak.

temperature ratio T_α/T_p, divided into five bins as indicated in each panel. Each distribution is normalized to its peak value. As the temperature ratio increases (from top to bottom in the figure), an evident shift of the distribution towards larger values of both ϵ_p and ϵ_α is observed; this shift can be clearly appreciated by looking at the location of the average value of T_α/T_p, indicated by a red dot in each panel of this figure. These results indicate that a larger deviation from a Maxwellian distribution is observed for larger temperature ratios T_α/T_p. On the other hand, the conditioned joint distributions are relatively symmetric, so that there is no evidence of different increase in ϵ_p or ϵ_α when the alpha particles are preferentially heated.

Temperature variations of the ions seem to be related to their kinetic dynamics and, therefore, to the complex deformations of the particle velocity distributions. Future space missions, such as THOR [60], designed to provide measurements of the three-dimensional ion distribution functions with very high phase space resolution, will be able to capture the non-Maxwellian deviations of the velocity distributions, so as to provide relevant clues on the long-standing problem of particle heating.

As discussed previously, close to the sites of enhanced magnetic activity, the non-Maxwellian measure ϵ_s achieves large values for both ion species. In order to show what the three-dimensional ion velocity distributions look like in turbulence, in figure 9 we report the iso-surfaces of the proton (panel (a)) and alpha particle (panel (b)) velocity distributions, computed in the spatial point where ϵ_s is maximum. The red tube in both panels indicates the direction of the local magnetic field. The proton velocity distribution displays a field-aligned beam and the generation of ring-like modulations in planes perpendicular to the direction of the local field, presumably signatures of cyclotron resonance. On the other hand, for the alpha particles we recovered more evident deformations, with the appearance of multiple blobs and elongations; the alpha particle velocity distribution seems to lose any property of symmetry with respect to the direction of the local magnetic field. It is clear from these plots that kinetic effects, working along the turbulent cascade at typical ion scales, can efficiently drive the plasma away from thermodynamic equilibrium. Moreover, when the particle velocity distributions are not constrained by limiting assumptions on their shape in velocity space, they can be distorted in a very complicated way and lose their symmetry.

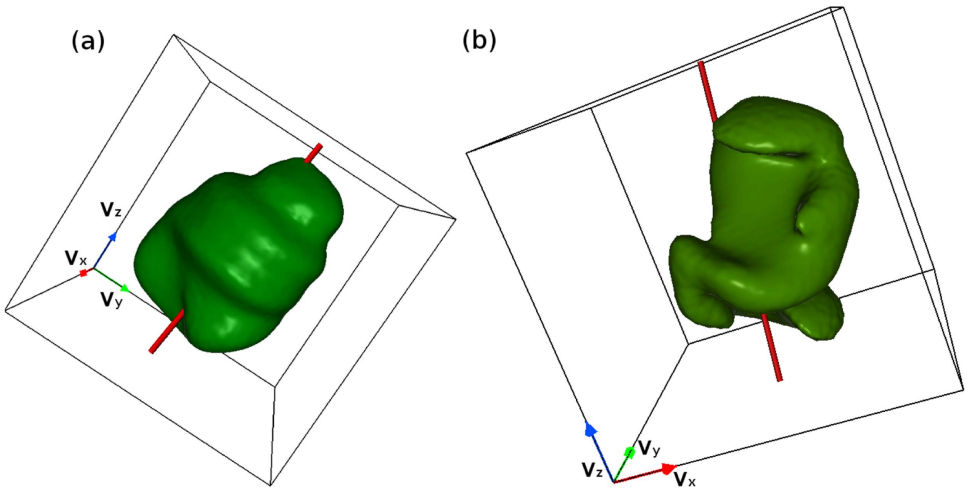

Figure 9. Iso-surfaces of the proton (panel (a)) and alpha particle (panel (b)) velocity distribution in a spatial point where ϵ_s is maximum. The direction of the local magnetic field vector is reported as a red tube.

5. Deviations from Maxwellian distributions

An alternative way to describe the deviations from thermodynamic equilibrium consists in defining the so-called minimum variance frame (MVF) of the three-dimensional velocity distribution. We compute the preferred directions of the velocity distribution of each ion species in velocity space [33], in each spatial position, from the stress tensor:

$$\Pi_{ij} = n^{-1} \int (v_i - u_i)(v_j - u_j) f \, \mathrm{d}^3 v. \tag{8}$$

This tensor can be diagonalized by computing its eigenvalues $\{\lambda_1, \lambda_2, \lambda_3\}$ (ordered in such way that $\lambda_1 > \lambda_2 > \lambda_3$) and the corresponding normalized eigenvectors $\{\hat{\mathbf{e}}_1, \hat{\mathbf{e}}_2, \hat{\mathbf{e}}_3\}$. We point out that λ_i are proportional to temperatures and $\hat{\mathbf{e}}_i$ are the anisotropy directions of the velocity distribution.

The quantity ϵ_s gives general information on the departure of the ion species from thermodynamic equilibrium, while the eigenvalues λ_i provide insights into the properties of symmetry of the ion velocity distributions. Therefore, for RUN 1 at $t = t^*$, we computed the PDF of the ratios λ_i/λ_j ($i, j = 1, 2, 3$ and $j \neq i$), conditioned to the values of $\epsilon_s(t = t^*)$. Note that each of these ratios is equal to unity for a Maxwellian velocity distribution. In figure 10, we show the PDF of λ_1/λ_2 (left panels), λ_1/λ_3 (middle panels) and λ_2/λ_3 (right panels) for protons (top row) and alpha particles (bottom row); these PDFs have been computed for three different ranges of values of ϵ_s, $0 \leqslant \epsilon_s \leqslant \hat{\epsilon}_{1,s}$ (black curve), $\hat{\epsilon}_{1,s} < \epsilon_s \leqslant \hat{\epsilon}_{2,s}$ (red curve) and $\hat{\epsilon}_{2,s} < \epsilon_s \leqslant \epsilon_{s,\max}$ (blue curve), where $\epsilon_{s,\max}$ represents the maximum value of ϵ_s over the two-dimensional spatial domain at $t = t^*$ ($\epsilon_{p,\max} = 0.17$, $\epsilon_{\alpha,\max} = 1.5$) and $\hat{\epsilon}_{1,p} = 0.04$, $\hat{\epsilon}_{2,p} = 0.07$, $\hat{\epsilon}_{1,\alpha} = 0.5$, $\hat{\epsilon}_{2,\alpha} = 1.0$.

From this latter figure it can be noticed that, in the range of small ϵ_s, the PDFs (for both protons and alphas) have a peak close to unity (they are not exactly centered around 1, since the minimum value of ϵ_s is not zero at $t = t^*$). As ϵ_s increases, high tails appear in the PDFs suggesting that, in the case of significant deviations from Maxwellian, the ion velocity distribution loses its properties of isotropy and gyrotropy. This observation suggests that the use of reduced models, based on restrictive approximations on the shape of the ion velocity distribution, might not be appropriate, and more complete models, describing the evolution of the velocity distributions in a full 3D velocity space, should be employed.

With the aim of characterizing the nature of the deformation of the particle velocity distributions and to identify the spatial regions which are the sites of kinetic activity, we computed for each ion species two indices of departure from Maxwellian, i. e. the temperature anisotropy index and the gyrotropy index, in two different reference frames, namely the MVF and the local magnetic field frame (LMF). We define the anisotropy measures $\zeta = |1 - \lambda_1/\lambda_3|$ (MVF) and $\zeta^* = |1 - T_\perp/T_\parallel|$ (LMF), where $T_\perp$ and $T_\parallel$ are the temperatures with respect to the local magnetic field, and the gyrotropy indicator in the MVF $\eta = |1 - \lambda_2/\lambda_3|$. The gyrotropy index in the LMF η^* can be computed by using the normalized Frobenius norm of the nongyrotropic part $\mathbf{N}$ of the full pressure tensor $\mathbf{\Pi}$ [73]:

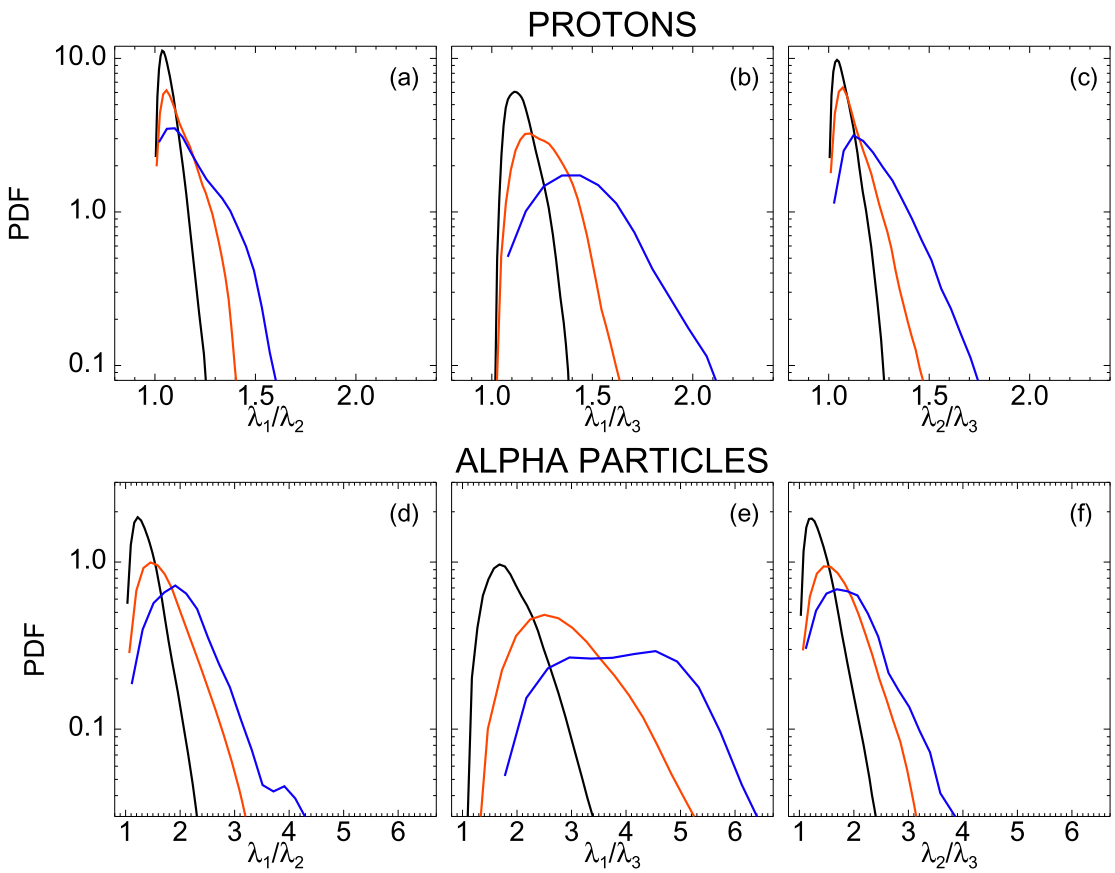

Figure 10. PDF of λ_1/λ_2 (panels (a) and (d)), λ_1/λ_3 (panels (b) and (e)) and λ_2/λ_3 (panels (c) and (f)) for both protons (top panels) and alpha particles (bottom panels). Each PDF has been computed for three different ranges of values of ϵ_s, namely $0 \leqslant \epsilon_s \leqslant \hat{\epsilon}_{1,s}$ (black curve), $\hat{\epsilon}_{1,s} < \epsilon_s \leqslant \hat{\epsilon}_{2,s}$ (red curve) and $\hat{\epsilon}_{2,s} < \epsilon_s \leqslant \epsilon_{s,\max}$ (blue curve).

$$\eta^* = \frac{\sqrt{\sum_{i,j} N_{ij}^2}}{\mathrm{Tr}(\mathbf{\Pi})}, \tag{9}$$

where N_{ij} are the components of the tensor $\mathbf{N}$, and $\mathrm{Tr}(\mathbf{N}) = 0$. It is worth to point out that all indices defined above are identically zero if the particle velocity distribution is Maxwellian. At the maximum of the turbulent activity, these indices significantly differ from zero for both ion species, meaning that the ion velocity distributions are anisotropic and non-gyrotropic in both MVF and LMF.

In figure 11, we show the spatial profiles of all these indices inside the region where the current sheet shown in figure 5 (b) is located (indicated by vertical black-dashed lines). The indices for protons are reported in the left panels, while for alpha particles in the right panels. As it is evident from this figure, the non-Maxwellian measures of both protons and alpha particles are not null in the regions close to the peak of the current density, in both reference frames; specifically, the ion velocity distributions become anisotropic and non-gyrotropic, as can be seen from both the MVF and LMF indices. It is worth noting that the indices for the alpha particles are significantly larger than for the protons, additional evidence that alpha particles are more efficiently driven out of equilibrium with respect to protons.

6. Optimized measurements for the study of protons and alpha particles kinetic dynamics

In the previous sections we have shown that kinetic effects produce highly non Maxwellian distributions, particle beams and ring-like modulations. An instrument designed to study these effects should have proper phase space (and temporal) resolution, since a poor resolution could impede the observations of such fine features. In near-Earth space it is possible to perform high resolution *in situ* plasma observations. Measurements of particle velocity distribution functions are usually performed by top-hat electrostatic analyzers [74]. Such instruments are composed of two concentric hemispheres set at different voltage, with an aperture on the outer hemisphere. The electric field between the plates allows for particles within a specific energy-per-charge (E/q) ratio to pass through the gap and reach the detector. Varying the voltage permits to sort particles according to their E/q. Parallel incident particles will be focused on a specific sector of the detector at the analyzer exit, each

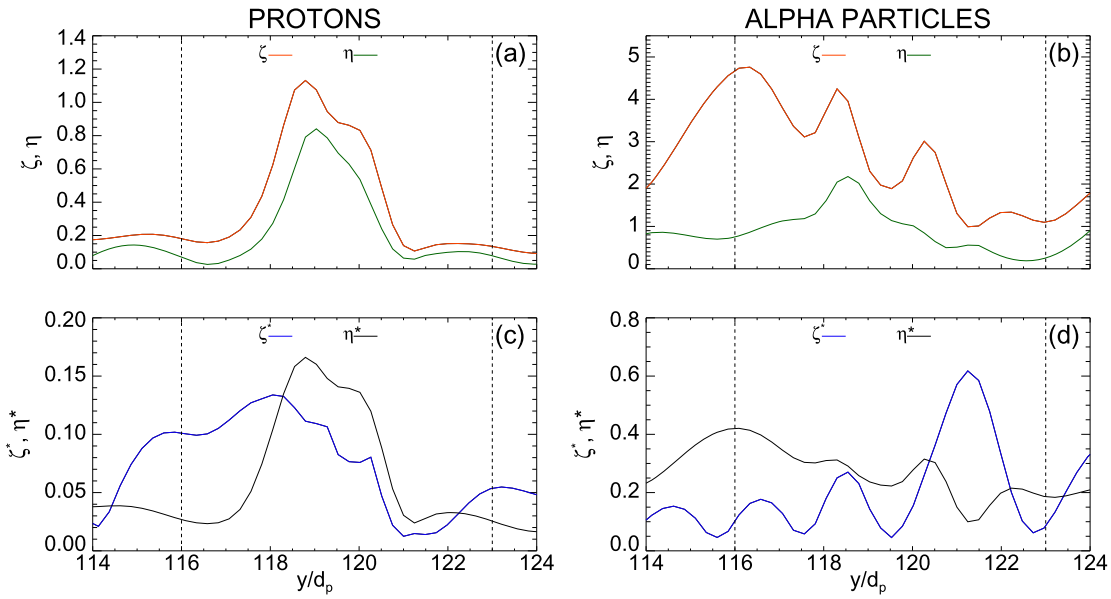

Figure 11. Temperature anisotropy indices ζ (red line) and ζ^* (blue line) and non-gyrotropy indices η (green line) and η^* (black line), for protons (left panels) and alpha particles (right panels), inside the current sheet in panel (b) of figure 5. Top and bottom panels refer to MVF and LMF, respectively.

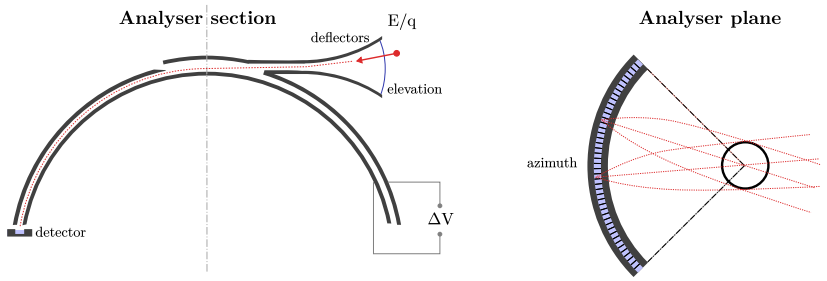

Figure 12. Schematic representation of a top-hat electrostatic analyzer specifically designed for measuring the solar wind proton and alpha distributions [59].

sector identifying the particle velocity azimuthal direction. Analyzers of this type measure incoming particles with a 360° disk shaped field of view. In order to sample the entire 4π solid angle, either the spacecraft rotation is used or electrostatic polar deflectors are employed. Usually analyzers for solar wind measurements are characterized by a restricted field of view, since the solar wind at 1 AU is a cold beam in velocity space. A schematic illustration of such a top-hat analyzer is given in figure 12.

As already said, the energy-angular resolution of the top-hat analyzer is extremely important when aiming to study the signatures of kinetic-scale processes, since low phase space resolution would smooth out the fine structures of the particles distribution functions. The CSW [59] on board the THOR mission is a top-hat analyzer conceived to measure solar wind protons and alpha particles distribution functions with unprecedented temporal and phase space resolutions [58, 59]. In particular, it has an angular and energy resolution that will permit to observe the fine structure characterizing the particle distribution functions related to the effects of turbulence.

In this respect, we use a *top-hat simulator* to find out how the proton and alpha velocity distributions characterized by large ϵ_s, and shown in figure 9, would be detected by CSW. Such distribution functions are meaningful examples since they are characterized by non Maxwellian shapes and a high degree of complexity as has been shown in the previous sections. Moreover, we compare the moments and the ϵ_s of the HVM and CSW distributions in proximity of large ϵ_s sites, showing that CSW measurements capture the complexity present in the HVM distributions.

CSW will detect particles in 96 energy-per-charge intervals with $\Delta E/E = 7\%$. It will have a restricted field of view of 48° in both azimuth and elevation, focused on the CSW population, and will have an unprecedentedly high angular resolutions of 1.5°, in both azimuth and elevation. The CSW response is further determined by its

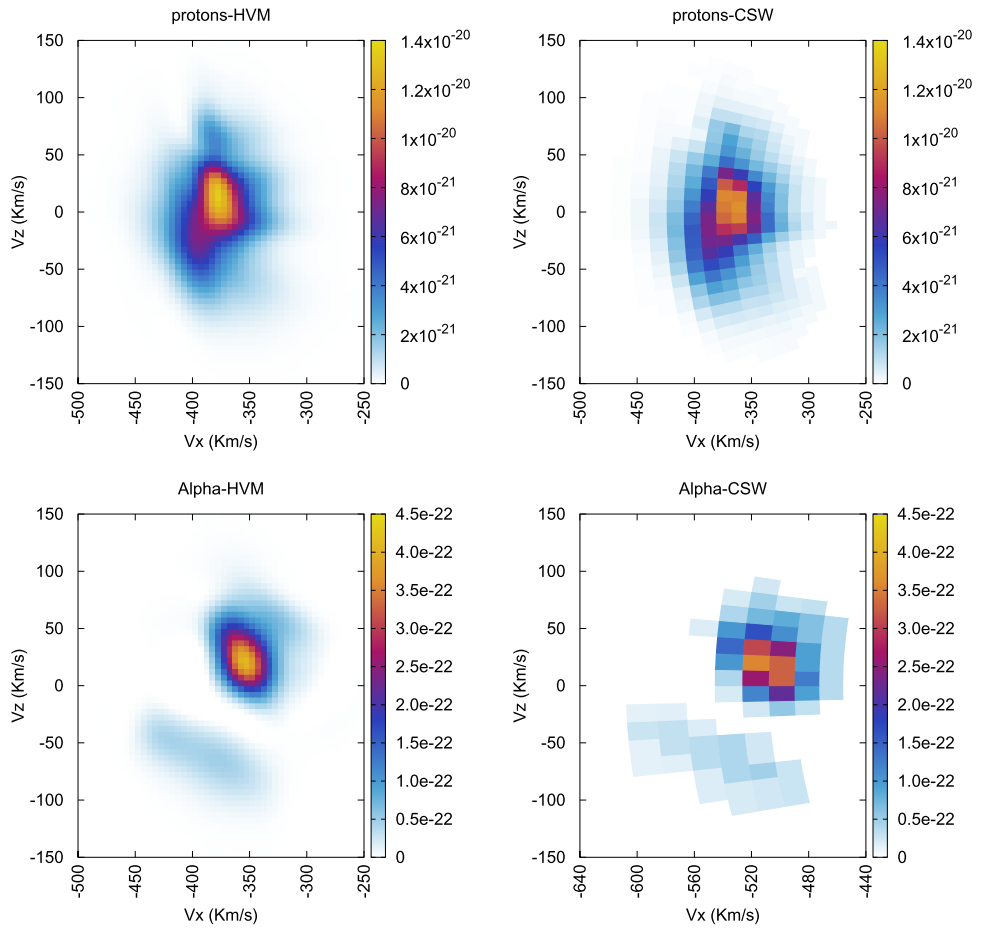

Figure 13. Protons and alpha particles velocity distributions as recovered from the simulations and as sampled by CSW. Note that the distribution function scale is not the same for protons and alphas.

geometric factor $G = 2.2 \times 10^{-5}$ cm^{2}sr and the time needed for the accumulation of particle counts in one energy channel and elevation angle $T_{\rm acc} \sim 0.25$ ms.

As a first step, the HVM distributions are expressed in physical units by rescaling the normalized variables of the simulation to physical quantities. In order to adapt to a real solar wind, a proton density of 8.2 cm^{-3}, a proton thermal velocity of 35 km s^{-1}, which corresponds to a thermal energy of 12.8 eV, and a $T_\alpha/T_p = 4$ have been used. Moreover, a bulk velocity of 400 km s^{-1} has been taken into account. Then the distribution functions are reassigned to the field of view of CSW by means of an averaging process. At this point, the counts that the sensors would detect in each energy-angular interval for each species are computed [75]:

$$\text{counts}_{i,j,k} = v_i^4 \cdot f_{i,j,k} \cdot T_{\rm acc} \cdot G, \tag{10}$$

where i, j, k refer to the energy, elevation and azimuth intervals, v_i is the velocity in the interval, f the distribution function, $T_{\rm acc}$ and G the accumulation time and the geometric factor, respectively. f is normalized in such a way that its integral in velocity space gives the particle number density. Afterwards, we determine the corresponding moments.

In figure 13 proton (top panels) and alpha (bottom panels) velocity distributions are shown at the spatial point where ϵ is maximum, as recovered from the HVM simulations (left panels) and as sampled by CSW (right panels). In particular, slices of the distribution functions in the $V_x V_z$ plane are presented.

Looking at the protons, it can be seen that all the features that characterize the HVM distribution are revealed by CSW. In fact, the ring-like modulations, that can be identified in the HVM distribution along the V_x direction, are present also in the CSW distribution, although they are less readily identifiable. Moreover, this distribution function spans only over one order of magnitude and will be easily observed by CSW for regular or dense solar wind.

Looking at the alpha particles, it has to be noted that the alphas population appears in the CSW distribution at $\sqrt{2}$ times the bulk velocity recovered from the simulation, since electrostatic analyzers like CSW detect particles with respect to their energy-per-charge. Regarding the features characterizing the HVM and CSW alpha distributions, it can be seen that the shape of the main alpha population, at about $(\boldsymbol{V_x}, \boldsymbol{V_z}) = (-340, 30)$,

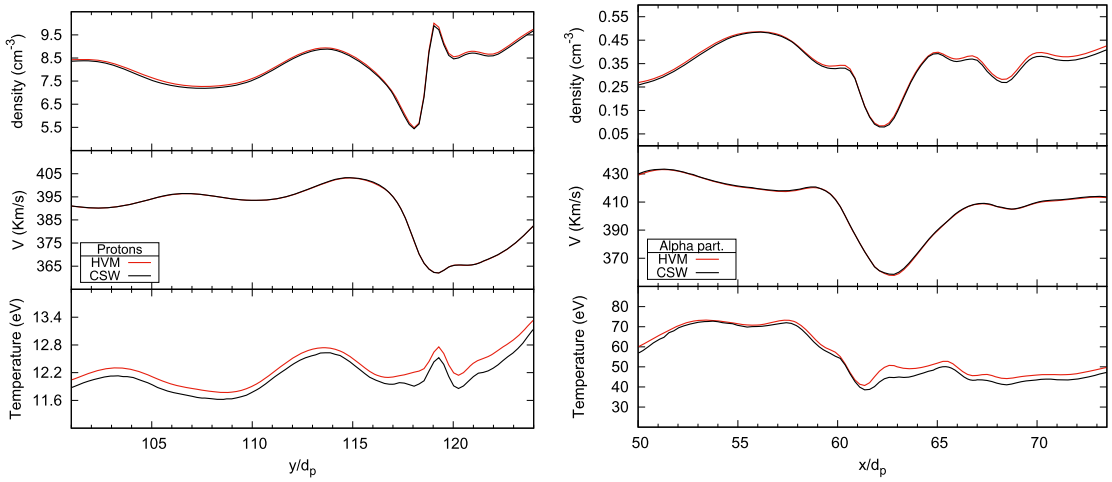

Figure 14. HVM (red lines) and CSW (black lines) density, velocity and temperature, computed for protons (left) and alpha particles (right) distributions along the y and x direction at $x_0 \simeq 60d_p$ and $y_0 \simeq 115d_p$, respectively.

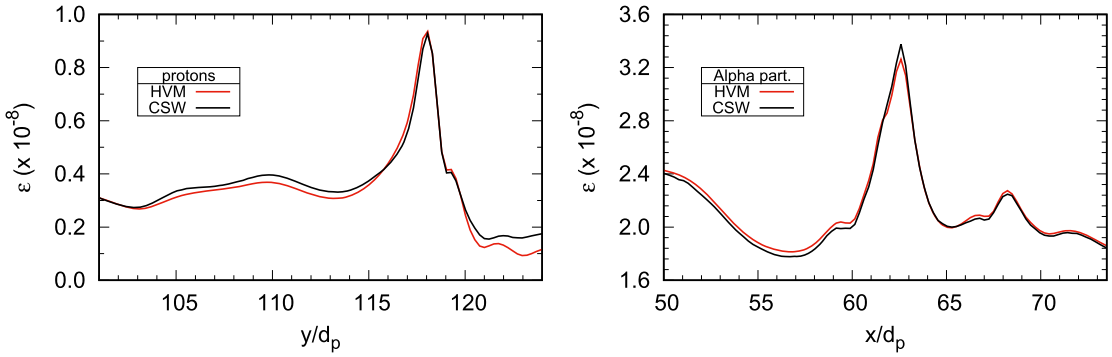

Figure 15. The non Maxwellian measure ϵ_s computed for the HVM (red line) and CSW (black line) distributions of protons (left panel) and alpha particles (right panel).

is correctly reproduced. In fact, the elongation visible in the HVM is clearly unveiled also in the CSW distribution, and also discernible is the faint widening on the left part of the core population. Moreover, the faint blob at negative V_z in the HVM distribution, is recognizable in the CSW distribution as well, and its shape is well captured.

In figure 14 we show the HVM (red lines) and CSW (black lines) density, velocity and temperature, for protons (left panel) and alpha particles (right panel), computed for distribution functions along the y and x direction at $x_0 \simeq 60d_p$ and $y_0 \simeq 115d_p$, respectively. Along these directions, the maximum ϵ_p and ϵ_α are encountered. Results show that the velocity, and to a lesser extent the density, for HVM and CSW are extremely well in agreement. Small differences can be noted between HVM and CSW temperature. The different behaviors of the temperature and lower order moments was already observed in [58]. In general, larger errors are found between the HVM and CSW moments for alpha particles than for protons. This can be explained in terms of the alpha particles lower counts statistics with respect to the protons.

Finally, the non Maxwellian measure ϵ_s, computed for the HVM (red line) and CSW (black line) distributions, is presented in figure 15. The ϵ_s evolution is the same for the HVM and CSW distributions. In particular, the two HVM ϵ_s peaks, of the protons and alphas cases, are well pronounced in the CSW ϵ_s evolution as well. The small difference between the peaks of the HVM and CSW ϵ_α can probably be explained in terms of the alphas lower counts statistics, like in the case of moments.

It must be noted here that, starting from the HVM simulation, the moments for the alpha particles can be readily computed. In the real case, although the alpha population can be easily identified in the CSW distribution functions, part of the protons and alpha particles populations can overlap, especially when the plasma temperature is high, and the moments computation can be hard (we recall that CSW selects particles according to their energy-per-charge). In such cases it is extremely useful to have a particle instrument that is able to

identify the different ion species. Such an instrument will be on board THOR: it is the ion mass spectrometer, a top-hat analyzer complemented with a time of flight section.

7. Summary and conclusions

We have employed a multi-component Eulerian HVM code to analyze the differential kinetic dynamics of the dominant ions in the turbulent solar wind. We have performed simulations of decaying turbulence in a five-dimensional phase space, varying relevant parameters, such as the level of turbulence and the plasma beta at equilibrium, in order to explore a large portion of the parameter space and to compare our numerical results with direct solar wind measurements. As the numerical results do not change qualitatively for the runs summarized in table 1, after showing that our simulations reproduce with a good degree of realism the phenomenology recovered in solar wind observations, we restricted our analysis to a single simulation.

We focused in particular on the departure of the plasma from thermodynamic equilibrium along the cascade and on the role of kinetic effects coming into play when the cascading energy reaches the typical ion scales. As turbulence develops, we observed the generation of ion temperature anisotropy with respect to the direction of the local magnetic field as well as a significant heating for both ion species. Also, the non-Maxwellian index ϵ_s, which is a measure of the deviations from Maxwellian of each ion species, gets different from zero; at the same time, the generation of coherent structures (current sheets, vortices, etc) of the typical width of few ion skin depths is observed in the contour map of the out of plane current density and of the ion vorticity. Generation of temperature anisotropy, particle heating and deformation of the ion velocity distributions clearly occur in the form of thin filaments at scales of the order of the ion kinetic scales.

A detailed statistical analysis of the simulation results provides evidence that the distribution of the numerical data is constrained to the stable region with respect to the fire-hose and mirror stability thresholds, evaluated by taking into account the multi-ion composition of the solar wind plasma. These results appear in good agreement with the observational evidences, recently discussed in [57].

The generation of temperature anisotropy and the process of particle heating are significantly more efficient for the alpha particles than for the protons and also the non-Maxwellian index gets larger values for the heavy ions. This means that not only a differential heating occurs, but also a differential kinetic behavior is observed for the dominant ion species in the solar wind: in fact, as shown in figure 9, the velocity distribution of the alpha particles appears much more distorted than that of the protons. Interestingly, the process of differential ion heating takes place close to the peaks of the ion vorticity and in spatial regions where the ion velocity distributions appear significantly distorted and far from thermodynamic equilibrium.

In order to characterize the deviations from Maxwellian, we analyzed the ion velocity distribution both in its minimum variance frame and in the local magnetic field frame, by defining the anisotropy and the gyrotropy indicators in both frames. The study of these indicators reveals that, when kinetic effects are at work and ϵ_s gets large, the shape of the velocity distributions of each ion species loses its symmetry, developing anisotropic and non-gyrotropic features. Moreover, close to the peaks of ϵ_s, sharp velocity gradients and complicated distortions are recovered.

If, as suggested by our numerical results, temperature variations of the ion species are related to the kinetic dynamics at short spatial scales, then the details of the velocity distribution, which keep the memory of the particle kinetic dynamics, are clearly crucial ingredients for the understanding of the complex process of particle heating. In fact, as we discussed above, different ion species, even though experiencing the same turbulent fields, exhibit a deeply different response, being heated and shaped differentially. By feeding a virtual top-hat analyzer with the ion velocity distributions obtained from the kinetic simulations discussed here, we have demonstrated that the energy and angular resolutions of the CSW instrument on board the THOR mission should allow to obtain unprecedentedly high resolution measurements of both proton and alpha velocity distributions and will therefore provide important information for unveiling the puzzling aspects of solar wind heating. The results discussed in this paper support the idea that future space missions, designed to provide measurements of particle velocity distributions and fields with very high resolution, will allow to gain relevant insights into the dynamics of the solar wind plasma at kinetic scales.

Acknowledgments

This work has been supported by the Agenzia Spaziale Italiana under the Contract No. ASI-INAF 2015-039-R.O 'Missione M4 di ESA: Partecipazione Italiana alla fase di assessment della missione THOR'. The numerical simulations discussed in the present paper have been performed on the Newton parallel machine at the Department of Physics at University of Calabria (Italy). Work at IRAP was supported by CNRS and CNES. DS and SS aknowledge support from the Faculty of the European Space Astronomy Centre (ESAC).

References

[1] Marsch E 2006 *Living Rev. Solar Phys.* **3** 1
[2] Richardson J D, Wang C and Burlaga L F 2003 *Geophys. Res. Lett.* **30** 2207
[3] Gazis P R and Lazarus A J 1982 *Geophys. Res. Lett.* **9** 431
[4] Borovsky J E and Gary S P 2014 *J. Geophys. Res.* **119** 5210
[5] Bruno R and Carbone V 2005 *Living Rev. Solar Phys.* **2** 4
[6] Bruno R and Carbone V 2013 *Living Rev. Solar Phys.* **10** 2
[7] Kolmogorov A N 1941 *Dokl. Akad. Nauk SSSR* **30** 301
[8] Coleman P J 1968 *Astrophys. J.* **153** 371
[9] Dobrowolny M, Mangeney A and Veltri P 1980 *Phys. Rev. Lett.* **45** 144
[10] Tu C-Y and Marsch E 1995 *Space Sci. Rev.* **73** 1
[11] Goldstein M L, Roberts D A and Matthaeus W H 1995 *Annu. Rev. Astron. Astrophys.* **33** 283
[12] Leamon R J, Matthaeus W H, Smith C W and Wong H K 1998 *Astrophys. J.* **507** L181
[13] Leamon R J *et al* 2000 *Astrophys. J.* **537** 1054
[14] Maksimovic M *et al* 2001 *Ann. Geophys.* **19** 1429
[15] Bale S D, Kellogg P J, Mozer F S, Horbury T S and Reme H 2005 *Phys. Rev. Lett.* **94** 215002
[16] Smith C W, Hamilton K, Vasquez B J and Leamon R J 2006 *Astrophys. J.* **645** L85
[17] Alexandrova O, Carbone V, Veltri P and Sorriso-Valvo L 2007 *Planet. Space Sci.* **55** 2224
[18] Matteini L *et al* 2007 *Geophys. Res. Lett.* **34** L20105
[19] Bourouaine S, Alexandrova O, Marsch E and Maksimovic M 2012 *Astrophys. J.* **749** 102
[20] Matthaeus W H, Zank G P, Oughton S, Mullan D J and Dmitruk P 1999 *Astrophys. J.* **523** L93
[21] Oughton S *et al* 2001 *Astrophys. J.* **551** 565
[22] Dmitruk P, Milano L J and Matthaeus W H 2001 *Astrophys. J.* **548** 482
[23] Hollweg J V and Isenberg P A 2002 *J. Geophys. Res.* **107** 1147
[24] Cranmer S R and van Ballegooijen A A 2003 *Astrophys. J.* **594** 573
[25] Cranmer S R and van Ballegooijen A A 2005 *Astrophys. J. Suppl. Ser.* **156** 265
[26] Cranmer S R, van Ballegooijen A A and Edgar R J 2007 *Astrophys. J. Suppl. Ser.* **171** 520
[27] Valentini F, Iazzolino A and Veltri P 2010 *Phys. Plasmas* **17** 052104
[28] Chandran B D G, Li B, Rogers B N, Quataert E and Germaschewski K 2010 *Astrophys. J.* **720** 503
[29] Bourouaine S and Chandran B D G 2013 *Astrophys. J.* **774** 96
[30] Greco A, Chuychai P, Matthaeus W H, Servidio S and Dmitruk P 2008 *Geophys. Res. Lett.* **35** L19111
[31] Osman K T, Matthaeus W H, Greco A and Servidio S 2011 *Astrophys. J.* **727** L11
[32] Osman K T, Matthaeus W H, Hnat B and Chapman S C 2012 *Phys. Rev. Lett.* **108** 261103
[33] Servidio S, Valentini F, Califano F and Veltri P 2012 *Phys. Rev. Lett.* **108** 045001
[34] Greco A, Valentini F, Servidio S and Matthaeus W H 2012 *Phys. Rev.* E **86** 066405
[35] Wu P *et al* 2013 *Astrophys. J.* **763** L30
[36] Matthaeus W H, Wan M, Servidio S, Greco A, Osman K T, Oughton S and Dmitruk P 2015 *Phil. Trans. R. Soc.* A **373** 20140154
[37] Kasper J C, Lazarus A J and Gary S P 2008 *Phys. Rev. Lett.* **101** 261103
[38] Tracy P J *et al* 2016 *Phys. Rev. Lett.* **116** 255101
[39] Isenberg P A and Vasquez B J 2009 *Astrophys. J.* **696** 591
[40] Perrone D, Valentini F and Veltri P 2011 *Astrophys. J.* **741** 43
[41] Valentini F, Perrone D and Veltri P 2011 *Astrophys. J.* **739** 54
[42] Cranmer S R and van Ballegoojen A A 2012 *Astrophys. J.* **754** 92
[43] Perrone D, Bourouaine S, Valentini F, Marsch E and Veltri P 2014 *J. Geophys. Res.* **119** 2400
[44] Araneda J A, Maneva Y G and Marsch E 2009 *Phys. Rev. Lett.* **102** 175001
[45] Maneva Y G, Vinas A F and Ofman L 2013 *J. Geophys. Res.* **118** 2842
[46] Ofman L, Vinas A F and Maneva Y G 2014 *J. Geophys. Res.* **119** 4223
[47] Maneva Y G, Ofman L and Vinas A F 2015 *Astron. Astrophys.* **578** A85
[48] Maneva Y G, Vinas A F, Moya P S, Wicks R T and Poedts S 2015 *Astrophys. J.* **814** 33
[49] Chandran B D G *et al* 2013 *Astrophys. J.* **776** 45
[50] Perrone D, Valentini F, Servidio S, Dalena S and Veltri P 2013 *Astrophys. J.* **762** 99
[51] Perrone D, Valentini F, Servidio S, Dalena S and Veltri P 2014 *Eur. Phys. J.* D **68** 209
[52] Perrone D *et al* 2013 *Space Sci. Rev* **178** 233
[53] Valentini F, Trávníček P, Califano F, Hellinger P and Mangeney A 2007 *J. Comp. Phys* **225** 753
[54] Valentini F *et al* 2014 *Phys. Plasmas* **21** 082307
[55] Servidio S *et al* 2014 *Astrophys. J.* **781** L27
[56] Servidio S *et al* 2015 *J. Plasma Phys.* **81** 325810107
[57] Chen C H K *et al* 2016 *Astrophys. J.* **825** L26
[58] De Marco R *et al* 2016 *J. Instrum.* **11** C08010
[59] Cara A *et al* 2016 Electrostatic analyzer design for solar wind proton measurements with high temporal, energy, and angular resolutions *J. Geophys. Res.* (submitted)
[60] Vaivads A *et al* 2016 *J. Plasma Phys.* **82** 905820501
[61] Peyret R and Taylor T D 1986 *Computational Methods for Fluid Flow* (New York: Springer)
[62] Mininni P D and Pouquet A 2009 *Phys. Rev.* E **80** 025401
[63] Sahraoui F, Goldstein M L, Robert P and Khotyaintsev Yu V 2009 *Phys. Rev. Lett.* **102** 231102
[64] Valentini F, Califano F and Veltri P 2010 *Phys. Rev. Lett.* **104** 205002
[65] Kunz M W, Schekochihin A A, Chen C H K, Abel I G and Cowley S C 2015 *J. Plasma Phys.* **81** 325810501
[66] Hellinger P 2007 *Phys. Plasmas* **14** 082105
[67] Maruca B A, Kasper J C and Gary P 2012 *Astrophys. J.* **748** 137
[68] Valentini F, Veltri P, Califano F and Mangeney A 2008 *Phys. Rev. Lett.* **101** 025006
[69] Valentini F and Veltri P 2009 *Phys. Rev. Lett.* **102** 225001
[70] Franci L, Hellinger P, Matteini L, Verdini A and Landi L 2006 *Proc. 14th Int. Solar Wind Conf.* vol 1720, p 040003

[71] Matthaeus W H 1982 *Geophys. Res. Lett.* **9** 660
[72] Parashar T N and Matthaeus W H 2016 *Astrophys. J.* **832** 57
[73] Aunai N, Hesse M and Kuznetsova N 2013 *Phys. Plasmas* **20** 092903
[74] Carlson C W, Curtis D W, Paschmann G and Michael W 1982 *Adv. Space Res.* **2** 67
[75] Paschmann G and Daly P W (ed) 1998 *ISSI Scientific Reports Series* ESA/ISSI 1 125